Monthly Notices
of the
ROYAL ASTRONOMICAL SOCIETY

MNRAS **519,** 1872–1880 (2023) https://doi.org/10.1093/mnras/stac3616

Particle acceleration in shearing flows: the self-generation of turbulent spine-sheath structures in relativistic magnetohydrodynamic jet simulations

Jie-Shuang Wang ,[1]★ Brian Reville ,[1] Yosuke Mizuno ,[2,3] Frank M. Rieger[1,4]
and Felix A. Aharonian[1,5,6]

[1] *Max-Planck-Institut für Kernphysik, Saupfercheckweg 1, D-69117 Heidelberg, Germany*
[2] *Tsung-Dao Lee Institute, Shanghai Jiao Tong University, 520 Shengrong Road, Shanghai 201210, China*
[3] *School of Physics and Astronomy, Shanghai Jiao Tong University, 800 Dongchuan Road, Shanghai 200240, China*
[4] *Institute for Theoretical Physics, University of Heidelberg, Philosophenweg 12, D-69120 Heidelberg, Germany*
[5] *Dublin Institute for Advanced Studies, 31 Fitzwilliam Place, Dublin 2, Ireland*
[6] *High Energy Astrophysics Laboratory, RAU, 123 Hovsep Emin St, Yerevan 0051, Armenia*

Accepted 2022 December 6. Received 2022 December 2; in original form 2022 November 9

ABSTRACT

X-ray observations of kiloparsec-scale extragalactic jets favour a synchrotron origin. The short cooling times of the emitting electrons require a distributed acceleration of electrons up to sub-PeV energies. In a previous paper, we found that this can be self-consistently explained by a shear acceleration model, where particles are accelerated to produce power-law spectra, with the spectral index being determined mainly by the velocity profile and turbulence spectrum. In this paper, we perform 3D relativistic magnetohydrodynamic simulations to investigate the formation of a spine-sheath structure and the development of turbulence for a relativistic jet propagating into a static cocoon. We explore different spine velocities and magnetic field profiles, with values being chosen to match typical Fanaroff–Riley type I/II jets. We find that in all cases a sheath is generated on the interface of the spine and the cocoon mainly as a result of the Kelvin–Helmholtz instability. The large-scale velocity profile in the sheath is close to linear. Turbulence develops in both the spine and the sheath, with a turbulent velocity spectrum consistent with Kolmogorov scaling. The implications for shear particle acceleration are explored, with a focus on the particle spectral index.

Key words: acceleration of particles – instabilities – MHD – galaxies: jets – X-rays: galaxies.

1 INTRODUCTION

Jets of active galactic nuclei (AGNs) are observed on all scales extending from the vicinity of the black hole event-horizon up to megaparsec distances (see Blandford, Meier & Readhead 2019, for a review). In large-scale AGN jets, bright diffuse X-ray emission has been observed out to distances of several hundreds of kiloparsecs (e.g. Harris & Krawczynski 2006). Numerous observations in recent years support a synchrotron origin of X-rays in nearby large-scale jets, for example optical polarimetry measurements (e.g. Cara et al. 2013; Georganopoulos, Meyer & Perlman 2016; Perlman et al. 2020) and GeV gamma-ray observations of some high-power Fanaroff–Riley (FR) type II jets (e.g. Meyer & Georganopoulos 2014; Meyer et al. 2015; Breiding et al. 2017). A synchrotron X-ray origin is certain in the case of the low-power FR I radio galaxy Centaurus A, as the same electrons produce the diffuse TeV emission (H. E. S. S. Collaboration et al. 2020).

A synchrotron origin of X-rays requires sub-PeV electrons in these large-scale jets; that is, the typical synchrotron photon energy is $E_{\rm syn} = 2(E_{\rm e}/0.1\ {\rm PeV})^2(B/10\ \mu{\rm G})$ keV, where B is the magnetic field strength. On the other hand, the synchrotron cooling time of a relativistic electron with energy $E_{\rm e}$ is $t_{\rm cool} = 1.25(E_{\rm e}/0.1\ {\rm PeV})^{-1}(B/10\ \mu{\rm G})^{-2}$ kyr, corresponding to a maximum cooling length of $\sim$0.4 kpc, decreasing further if the magnetic fields are higher. The observed X-ray structures of large-scale jets have sizes exceeding a kiloparsec(e.g. Harris & Krawczynski 2006), indicating that an *in situ* (re-)acceleration mechanism is required. Shear particle acceleration can serve as a natural explanation (Liu, Rieger & Aharonian 2017; Wang et al. 2021; Tavecchio 2021). In our previous work (Wang et al. 2021), we obtained an exact solution of the steady-state Fokker–Planck equation for shear acceleration in the presence of synchrotron losses, and found that the particle distribution resembles a power law with an exponential-like cutoff. The corresponding synchrotron radiation from such a population of electrons was shown to reproduce the observed optical-to-X-ray spectral energy distributions (SEDs) of Centaurus A and 3C 273.

★ E-mail: jswang@mpi-hd.mpg.de

© The Author(s) 2022.
Published by Oxford University Press on behalf of Royal Astronomical Society. This is an Open Access article distributed under the terms of the Creative Commons Attribution License (http://creativecommons.org/licenses/by/4.0/), which permits unrestricted reuse, distribution, and reproduction in any medium, provided the original work is properly cited.

Downloaded from https://academic.oup.com/mnras/article/519/2/1872/6965859 by DESY-Zentralbibliothek user on 03 February 2023

Shear acceleration is naturally expected in fast, velocity-shearing flows. It can be understood as a second-order Fermi-type acceleration mechanism, where particles can gain energy by scattering on the turbulence embedded in the velocity-shear flows (Berezhko 1981; Berezhko & Krymskii 1981; Earl, Jokipii & Morfill 1988; Rieger & Duffy 2004; Rieger, Bosch-Ramon & Duffy 2007; Rieger & Duffy 2016; Webb et al. 2018, 2019; Rieger 2019). The resulting accelerated particle spectrum depends mainly on the velocity profile and turbulence spectrum (Liu et al. 2017; Webb et al. 2018, 2019, 2020; Rieger & Duffy 2019, 2021, 2022; Wang et al. 2021). Observationally, the existence of such velocity-shear layers (or sheaths) has been supported by high-resolution radio imaging and polarization studies of large-scale jets (e.g. Laing & Bridle 2014; Gabuzda, Reichstein & O'Neill 2014; Nagai et al. 2014; Boccardi et al. 2016; Blandford et al. 2019). However, the detailed properties of such velocity-shearing sheaths remain to be studied.

One way of doing this is through relativistic magnetohydrodynamic (RMHD) simulations. RMHD simulations have been extensively conducted to study the dynamics of relativistic jets (see Martí 2019, for a recent review). The interaction between a jet and its ambient medium has been explored to study the global jet stability and morphology, and the formation of a hot cocoon and the development of MHD instabilities can clearly be observed (e.g. Martí et al. 1997; Komissarov 1999; Scheck et al. 2002; Perucho & Martí 2007; Rossi et al. 2008; Mignone et al. 2010; Tchekhovskoy & Bromberg 2016; Rossi et al. 2017; Perucho, Martí & Quilis 2019; Mukherjee et al. 2020). Typically, in these simulations the numerical resolution in the jet region is severely limited owing to the large simulation domain, and it is usually inadequate for following the MHD instabilities accurately.

Dedicated analytical and numerical studies have also been performed to study the properties of MHD instabilities in jets. Two instabilities of importance are the Kelvin–Helmholtz instability (KHI), which can occur with or without magnetic fields near the interface of the velocity shear region (e.g. Ferrari, Trussoni & Zaninetti 1978; Hardee 1979; Birkinshaw 1991; Baty & Keppens 2002; Perucho et al. 2004; Mizuno, Hardee & Nishikawa 2007; Bodo et al. 2013, 2019; Sironi, Rowan & Narayan 2021; Borse et al. 2021; Chow, Davelaar & Sironi 2022), and the current-driven instability (CDI), which occurs in the presence of toroidal magnetic fields (e.g. Lyubarskii 1999; Nakamura, Li & Li 2007; Hardee 2007; Mizuno et al. 2009, 2012; Mizuno, Hardee & Nishikawa 2014; Kim et al. 2018; Bromberg et al. 2019; Ortuño-Macías et al. 2022), although see Gourgouliatos & Komissarov (2018). In general, CDI dominates in high-magnetization jets, while KHI dominates in low-magnetization jets, although the interaction between the CDI and KHI may also provide a stabilizing effect in low-magnetization jets (e.g. Baty & Keppens 2002). In addition, kinetic plasma simulations are utilized to investigate both the jet dynamics and particle acceleration through the dissipation of magnetic energy (e.g. Sironi et al. 2021; Ortuño-Macías et al. 2022). It has been suggested that these accelerated particles can serve as seed particles for shear acceleration (e.g. Wang et al. 2021).

In this paper, we investigate the self-generation of a sheath by simulating a relativistic spine jet propagating into a static cocoon using 3D RMHD simulations. We study the resultant jet properties, including the developed turbulence and possible shear acceleration. In Section 2, we introduce the parameters and initial conditions for our simulations, and show the results on the jet dynamics. In Section 3, we analyse the velocity and turbulence properties and discuss the implications for shear acceleration. The conclusions and a discussion are presented in Section 4.

2 NUMERICAL SETUP AND THE JET DYNAMICS

2.1 Numerical setup

We perform a numerical study of relativistic magnetized jet-spine flows propagating within a surrounding cocoon in order to investigate the properties of the self-generated spine-sheath structure. The PLUTO code (Mignone et al. 2007) is employed to solve the RMHD equations in 3D Cartesian geometry. We adopt a Taub–Mathews equation of state (Mathews 1971; Mignone, Plewa & Bodo 2005; Mignone et al. 2007), where the specific enthalpy is $h = 5\Theta/2 + \sqrt{9\Theta^2/4 + 1}$ and $\Theta = p_{\rm g}/\rho c^2$ represents the dimensionless temperature, with $p_{\rm g}$ and ρ being the thermal gas pressure and density, respectively.

The jet is initialized as a cylindrical flow with a spine radius (R_0) and its symmetry axis parallel to the y-axis. The boundary conditions are periodic in the y-direction, mimicking a jet of infinite extent, with outflow boundary conditions used at the other simulation boundaries. The jet rest-mass density is $\rho_0 = n_0 m_{\rm p}$, with $n_0 = 10^{-6}$ and $m_{\rm p}$ being the proton mass. The jet propagates into a hot stationary cocoon, which is formed with a density $\rho_{\rm c} = 2\rho_0$ (e.g. Mukherjee et al. 2020) owing to the interaction between the jet and the ambient medium. The density profile in the cocoon ($r > R_0$) is smoothed according to $\rho = (\rho_{\rm c} - \rho_0)\tanh\,[(r/R_0 - 1)/0.01] + \rho_0$. The velocity is only assigned within R_0 to ensure that energy is injected only in this region.

To facilitate our study of the turbulent jet dynamics, we introduce small transverse velocity field perturbations on the jet–cocoon interface following the approach of Rossi et al. (2008):

$$(\beta_x, \beta_z) = \frac{\tilde{A}}{24}\sum_{m=0}^{2}\sum_{l=1}^{8}\cos(m\phi + k_l y)(\cos\phi, \sin\phi), \tag{1}$$

with

$$k_l = \frac{(0.5, 1, 2, 3, 0.03, 0.06, 0.12, 0.25)}{\beta_0\sqrt{1/\Upsilon\Theta + 1/(\Upsilon - 1)}}$$

and $\Upsilon = 13/9$. The transversal component of velocity is $\beta_{x,\,z} = v_{x,\,z}/c$. The azimuth is defined as $\phi = \tan^{-1}(z/x)$. The perturbation amplitude is $\tilde{A} = \sqrt{\epsilon + 0.5\epsilon^2}/\,\Gamma_0(1 + \epsilon)$, where we set $\epsilon = 0.001$ for all simulations.

A helical magnetic field configuration is initialized in both the spine and the cocoon. The field consists of an axial component B_y and a toroidal component B_ϕ, where

$$B_y = \frac{B_1}{1 + (r/a)^2},$$
$$B_\phi = \frac{B_2(r/a)}{1 + (r/a)^2}, \tag{2}$$

with $a = R_0/2$ (e.g. Mizuno et al. 2009). This choice results in a constant pitch parameter $\Pi = rB_y/B_\phi = aB_1/B_2$. The normalization parameters B_1 and B_2 determine the mean magnetization parameter of the axial and toroidal components,

$$\sigma_{y,\phi} =< B^2_{y,\phi} > /8\pi\rho_0 c^2, \tag{3}$$

with the mean value given by $< f >= \int_0^{R_0} 2\pi f r{\rm d}r/\int_0^{R_0} 2\pi r{\rm d}r$. The magnetization inside the spine is then $\sigma = \sigma_y + \sigma_\phi$.

The magnetic field profile matches a screw pinch configuration, for which the equilibrium condition is

$$B_\phi \frac{u\partial(rB_\phi)}{\partial r} + rB_y\frac{\partial B_y}{\partial r} + 4\pi r\frac{\partial p_{\rm g}}{\partial r} = 0. \tag{4}$$

Downloaded from https://academic.oup.com/mnras/article/519/2/1872/6965859 by DESY-Zentralbibliothek user on 03 February 2023

Table 1. The initial parameters used in the simulations. The grid size is fixed at $0.016R_0$ except for case V6B-1-LR, which uses a lower resolution (LR). We also test the effect of box size by setting a smaller box (SB) length in the V6B-1-SB case.

Runs*	β_0	σ_y	σ_ϕ	Box size	Grid points	Θ_0	R_0	$L_{\rm K}$(erg s^{-1})
V6B-1	0.6	10^{-1}	10^{-1}	$6.0R_0$	375^3	0.01	0.1kpc	1.3×10^{43}
V6B-1-SB	0.6	10^{-1}	10^{-1}	$4.8R_0$	300^3	0.01	0.1kpc	1.3×10^{43}
V6B-1-LR	0.6	10^{-1}	10^{-1}	$6.0R_0$	200^3	0.01	0.1kpc	1.3×10^{43}
V6B-2	0.6	10^{-2}	10^{-2}	$6.0R_0$	375^3	0.01	0.1kpc	1.3×10^{43}
V6BA-2	0.6	0.016	0.004	$6.0R_0$	375^3	0.01	0.1kpc	1.3×10^{43}
V6BT-2	0.6	0.004	0.016	$6.0R_0$	375^3	0.09	0.1kpc	1.6×10^{43}
V6B-3	0.6	10^{-3}	10^{-3}	$6.0R_0$	375^3	0.01	0.1kpc	1.3×10^{43}
V9B-1	0.9	10^{-1}	10^{-1}	$8.0R_0$	500^3	0.09	1 kpc	6.7×10^{45}
V9B-2	0.9	10^{-2}	10^{-2}	$8.0R_0$	500^3	0.04	1 kpc	7.0×10^{45}
V9B-3	0.9	10^{-3}	10^{-3}	$8.0R_0$	500^3	0.02	1 kpc	6.7×10^{45}
V99B-2	0.99	10^{-2}	10^{-2}	$8.0R_0$	500^3	0.07	1 kpc	7.9×10^{46}

Note. *Terminology: V stands for the jet spine velocity; BA/BT/B indicates that the magnetic field is dominated by the axial/toroidal/both components.

The gas pressure can be shown to satisfy

$$p_{\rm g} = p_{\rm g,0} + \frac{B_1^2 - B_2^2}{8\pi}\left(1 - \frac{1}{(1 + (r/a)^2)^2}\right), \qquad (5)$$

where $p_{\rm g,\,0} = \Theta_0 \rho_0 c^2$ is the gas pressure at $r = 0$.

The initial values of the jet velocity ($\beta_y = v_y/c = \beta_0$), magnetization ($\sigma$), and temperature ($\Theta_0$) for each case are listed in Table 1. We choose to study three initial velocities, with $\beta_0 = 0.6$ (labelled V6) for a typical FR I jet, and $\beta_0 = 0.9$ and 0.99 (labelled V9 and V99) for FR II jets. The corresponding kinetic luminosity ($L_{\rm K} = \pi R_0^2 v_y \Gamma_0^2 \rho_0 h c^2$) is also shown in Table 1, where Γ_0 is the jet bulk Lorentz factor. To explore the effect of the magnetic field, we study three magnetization values, with $\sigma_y = 10^{-1},\ 10^{-2},\ 10^{-3}$ (labelled B-1, B-2, and B-3) and an axial/toroidal field-dominated case (labelled V6BA-2/V6BT-2). According to equation (3), the jet average magnetic field is $\bar{B}_0 = \sqrt{2\sigma}B_0 = 194\sqrt{\sigma}\mu$G in our simulations, with $B_0 = \sqrt{4\pi\rho_0 c^2} = 137\mu$G.

The jets are assumed to be cold with $\Theta_0 = 0.01{-}0.09$, where we adopt higher temperatures for magnetically dominated jets to avoid negative pressure (see equation 5). The averaged magnetic pressure in the spine is $p_B = \sigma\rho_0 c^2$, which along with equation (3) indicates that $p_B/p_{\rm g} = \sigma/\Theta$. Therefore, the jet pressure is comparable with the gas pressure when $\sigma \sim \Theta_0$. Thus, in our setup of $\Theta_0 = (0.01{-}0.09)$, $\sigma = 0.02$ implies that the magnetic pressure is comparable to the gas pressure, while $\sigma = 0.2$ and $\sigma = 0.002$ mean magnetic- or gas-pressure-dominated, respectively.

It has been found that, for cold jets, the KHI dominates in low-magnetization jets and the CDI can dominate in high-magnetization jets (Bodo et al. 2013). In our simulations, we also find that the CDI is dominant in the V6BT-2 and V9B-1 cases with a low temperature $\theta_0 \lesssim 0.05$, leading to a strong deceleration of the jet spine. However, as we are interested mainly in the development of the sheath caused by the KHI, we adopt a slightly higher temperature ($\theta_0 = 0.09$) for the V6BT-2 and V9B-1 cases to avoid the domination of the CDI.

2.2 Results on jet dynamics

The global behaviour of the time evolution of the simulations is similar in different cases. Owing to the application of strong toroidal fields in Cartesian geometry, the initial configuration is not in exact pressure balance, resulting in a transient, short-lived period of relaxation. Following this, the small perturbations imposed on the transition layer between the jet and the cocoon lead to the growth of the KHI driven by the velocity shear in this layer. Fig. 1 shows the time evolution of the non-axial component of the kinetic energy, $E_{\rm K,\perp} \equiv \rho c^2(\beta_x^2 + \beta_z^2)/2$, which is used to indicate the development of the KHI. In the linear stage, we see the exponential growth of the non-axial component of the kinetic energy, and large eddies gradually develop at the transition layer. The turbulence developed by eddies will amplify the magnetic field locally. In the saturation stage, the system tends to evolve non-linearly. The CDI may also grow in this stage and help to saturate the KHI (Baty & Keppens 2002). The pressure imbalance at the transition layer will affect the jet and the cocoon in this stage, and can generate shocks and waves. The transition layer becomes fully turbulent in the later stage of the simulations. An example of the velocity and magnetic field structure at this stage is shown in Fig. 2. The detailsare further explored in Section 3.2.

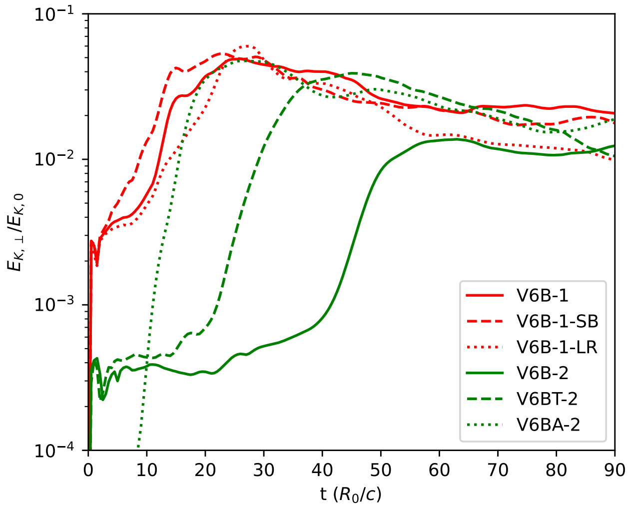

Figure 1. The non-axial component of the kinetic energy $E_{\rm K,\perp} \equiv \rho c^2(\beta_x^2 + \beta_z^2)/2$ is used to indicate the development of the KHI. The kinetic energy is defined in the Newtonian approximation and is normalized to the initial kinetic energy $E_{\rm K,\,0}$. We test the effects of simulation box size and resolution with the cases V6B-1, V6B-1-SB, and V6B-1-LR. The V6B-2, V6BT-2, and V6BA-2 cases are used to study the effect of the magnetic field configurations.

To assess the validity of the results on the large-scale dynamics that follow, including the influence of the boundaries as well as of grid resolution, we explore different box sizes ($4.8R_0$, $6.0R_0$) and

Downloaded from https://academic.oup.com/mnras/article/519/2/1872/6965859 by DESY-Zentralbibliothek user on 03 February 2023

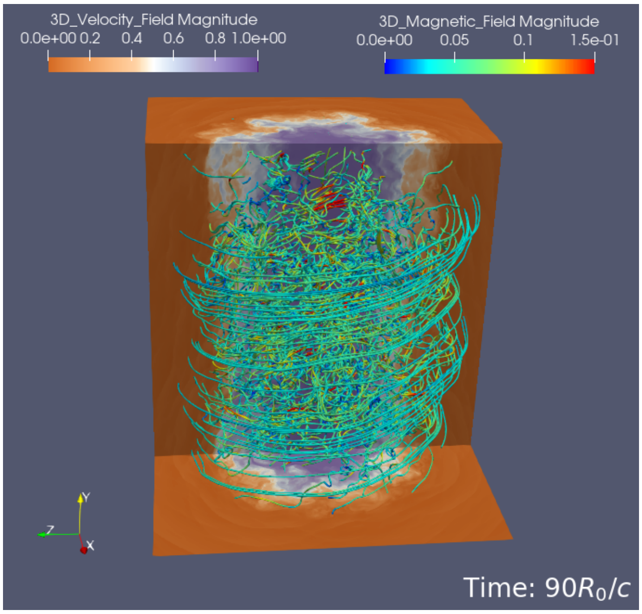

Figure 2. An example of the simulation results: the 3D velocity (β) magnitude distribution and the magnetic field-lines ($\vec{B}$) in 3D are shown for the V9B-3 case at $t = 90R_0/c$. The magnetic field is normalized to $B_0 = \sqrt{4\pi\rho_0 c^2} = 137\,\mu\text{G}$.

grid resolutions ($0.016R_0$, $0.03R_0$). The case V6B-1 is the reference case, for which we use a box size of $6.0R_0$ and a grid resolution of $0.016R_0$ (see Table 1). In the cases of V6B-1-SB and V6B-1-LR, a smaller box size and a lower grid resolution are used, respectively. We find that the box size has a negligible effect on the development of the KHI, provided it exceeds the width of the generated spine-sheath structure (see Section 3 for more details). The resolution is seen to have an effect on both the growth and the saturation stage of the KHI. In the lower-resolution case, the growth rate is slightly smaller, and $E_{\mathrm{K},\perp}$ is mildly suppressed in the saturation stage. Thus, in the following work we adopt a high resolution with a grid size of $0.016R_0$ and a box size of $6R_0$ for FR I jets ($\beta_0 = 0.6$) and of $8R_0$ for FR II jets ($\beta_0 \geq 0.9$), corresponding to uniformly spaced computational domains with 375^3 cells and 500^3 cells, respectively.

We examine the axial velocity profile as a function of radius to measure the spine-sheath structure. In the left-hand panel of Fig. 3, we show the velocity profiles of the V6B-2 case at different locations along y. It is evident that a shearing layer is formed between the jet and the cocoon as a result of the KHI: a spine-sheath structure is generated. Because the velocity profile varies along the jet axis, we use the averaged velocity profile to represent the generated spine-sheath structure. The sheath is defined as the layer in which the velocity decreases continuously, which is approximately in the range $\sim 0.8R_0 - 1.3R_0$, as shown in Fig. 3. The spine is the region enclosed by the sheath. In the right-hand panel we show the averaged profile at different simulation times. The velocity profile at the early stage of the KHI development ($t = 30R_0/c$) differs only slightly from the initial setup, and the jet width continues to expand in the saturation stage ($t = 60,\ \ 90R_0/c$), indicating the location and extent of the sheath.

We simulate three different magnetic configurations for FR I jets with $\sigma = 0.02$ to investigate the effect of the magnetic field configuration: an equal-field case (V6B-2 with $\sigma_y = \sigma_\phi$), an axial-field-dominated case (V6BA-2), and a toroidal-field-dominated case (V6BT-2), where the temperature Θ_0 is the same for the V6B-2 and V6BA-2 cases, and a higher temperature is assigned for V6BT-2 to avoid negative pressure (see equation 5). Fig. 1 shows that the KHI has a different growth rate in different cases. This is because a high toroidal field (Baty & Keppens 2002) or a low temperature (Hardee 2007) tends to suppress the KHI. The V6B-2 and V6BT-2 cases experience longer relaxation times owing to the larger applied toroidal fields. In the early saturation stage shown in Fig. 4, the velocity and magnetic field profiles deviate slightly from the initial setup. Fig. 4 also shows that the V6BA-2 and V6BT-2 cases have sheaths that are slightly wider than those for the V6B-2 case. However, the difference is insignificant in the velocity profiles. We thus fix $\sigma_y = \sigma_\phi$ in the following studies.

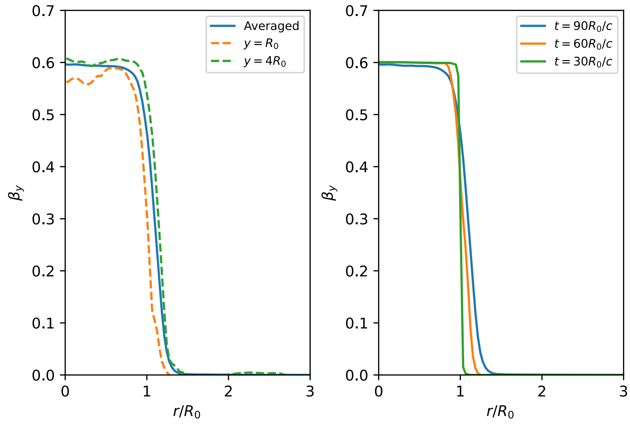

Figure 3. The azimuthally averaged axial velocity profiles for the V6B-2 case as a function of radius. Left-hand panel: profiles at fixed time $t = 90R_0/c$. The solid line shows the axial velocity averaged in the y-direction over the full length of the box. For comparison, we show examples of the profiles at two fixed points along the jet, at $y = R_0$ and $4\,R_0$. Right-hand panel: the y-averaged velocity profiles at different simulation times.

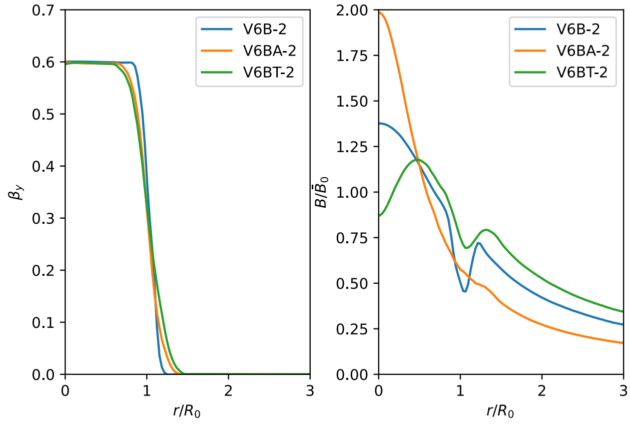

Figure 4. The azimuthally and y-averaged velocity (left-hand panel) and magnetic field (right-hand panel) profiles for the cases V6B-2 at $t = 60R_0/c$, V6BT-2 at $t = 40R_0/c$, and V6BA-2 at $t = 20R_0/c$.

We consider three magnetization scenarios, with $\sigma_y = \sigma_\phi = 10^{-1}$, 10^{-2}, 10^{-3} for both FR I ($\beta_0 = 0.6$) and FR II ($\beta_0 = 0.9$) jets to explore the impact of magnetization. We also study one more highly relativistic case, namely V99B-2 with $\beta_0 = 0.99$ and $\sigma_y = \sigma_\phi = 10^{-2}$, to investigate the effect of spine velocity. The evolution of the KHI in these jets is shown in Figs 1 and 5. We simulate these jets up to the late saturation stage to determine the spine-sheath properties and their implication for shear acceleration.

Downloaded from https://academic.oup.com/mnras/article/519/2/1872/6965859 by DESY-Zentralbibliothek user on 03 February 2023

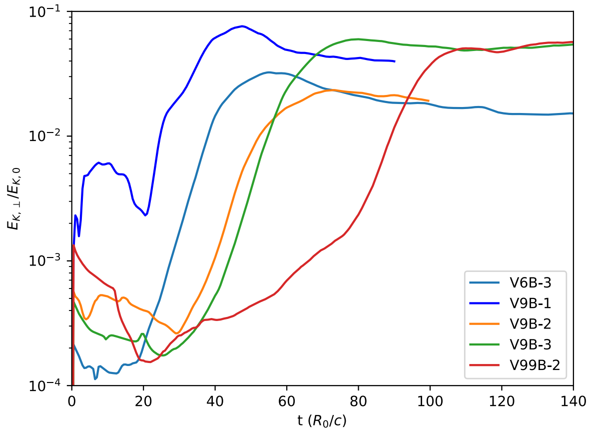

Figure 5. Plot, similar to Fig. 1, showing the non-axial component of the kinetic energy $E_{\mathrm{K},\perp} \equiv \rho c^2(\beta_x^2 + \beta_z^2)/2$ to the initial kinetic energy $E_{\mathrm{K},0}$ to indicate the growth rate of the KHI for the cases V6B-3, V9B-1, V9B-2, V9B-3, and V99B-2.

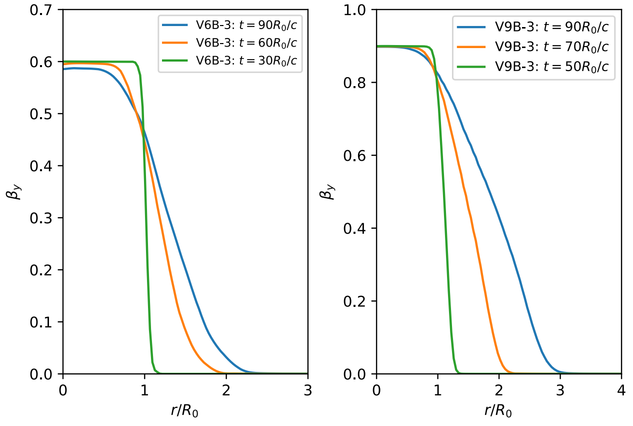

Figure 6. The evolution of the averaged axial velocity profile at different stages of development of the KHI for cases V6B-3 (left-hand panel) and V9B-3 (right-hand panel).

3 RESULTS ON AND IMPLICATIONS OF SHEAR ACCELERATION

Shear acceleration can be understood as a stochastic-type Fermi acceleration mechanism, where particles are accelerated via scattering off the turbulence embedded in the shearing flows. In a previous paper (Wang et al. 2021), we studied the steady-state Fokker–Planck equation for shear acceleration and obtained an exact solution for the particle spectrum. The spectrum consists of a power-law component with an exponential-like cutoff, where the power-law index is determined by the turbulence spectral index and the velocity profile (equations 10, 11 and 3 in Wang et al. 2021). In this paper, we study such properties for simulated jets with self-generated spine-sheath structures.

3.1 Velocity and magnetic field profiles

We first study the evolution of velocity profiles in the linear stage, the transition stage, and the deep saturation stage of the KHI. The choices of simulation time for these stages are based on the evolution of $E_{\mathrm{K},\perp}$ in Figs 1 and 5. Two examples, cases V6B-3 and V9B-3, are shown in Fig. 6. In the early stage, the profile does not deviate much from the initial setup. The shrinking of the jet spine and the development of a sheath can be clearly observed in the transition stage, and the trend continues in the saturation stage owing to the pressure imbalance induced by the saturated KHI.

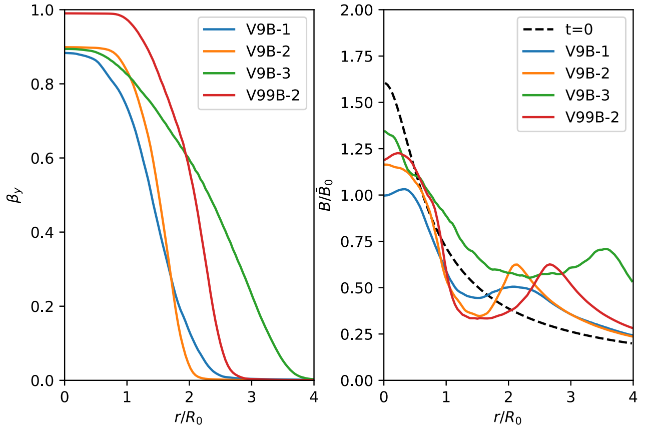

Figure 7. The axial velocity profiles (left-hand panel) and magnitude of the magnetic field profiles (right-hand panel) for FR II jets at $t = 90R_0/c$ (V9B-1), $t = 100R_0/c$ (V9B-2), $t = 120R_0/c$ (V9B-3), and $t = 120R_0/c$ (V99B-2). The magnetic field is normalized to $\tilde{B}_0 = \sqrt{2\sigma}B_0$.

We next focus on the jet velocity and magnetic field profiles in the deep saturation stage. The velocity and magnetic field profiles for FR II jets are shown in Fig. 7. Our results show that the gas-pressure-dominated (V9B-3) jet has the widest jet profile, while the jet widths are roughly comparable in those cases with a significant contribution of magnetic pressure (V9B-1 and V9B-2). In the V9B-3 case, the jet sheath grows to $W_{\mathrm{sh}} \sim 3.1R_0$ with a spine radius $R_{\mathrm{sp}} \sim 0.6R_0$. In the V9B-1 and V9B-2 cases, the sheath widths are $W_{\mathrm{sh}} \sim 1.3{-}2.0R_0$ with spine radii $R_{\mathrm{sp}} \sim 0.5{-}0.8R_0$. The spine velocity profiles are rather flat, while the sheath exhibits a smoothly decreasing velocity profile. Compared with the V9B-2 case, the V99B-2 case reveals a significantly wider sheath ($W_{\mathrm{sh}} \sim 2.0R_0$) but has a similar spine width in the deep saturation stage.

For the magnetic field profiles, we also show the initial profile at $t = 0$ in the right-hand panel of Fig. 7, which is identical in all cases. The magnetic field is reduced in the spine, while it is enhanced within and even beyond the sheath in the saturated KHI stage, with a considerable pile up of magnetic field at the sheath edge in all cases. In higher-magnetization cases, the magnetic field in the spine decreases further, and its pile-up effect at the sheath edge is weaker. In addition, a global amplification of the magnetic field is evident in the gas-pressure-dominated case (V9B-3), with a more uniform sheath magnetic field profile.

The results for the simulated FR I jets in the deep KHI saturation stage are shown in Fig. 8. As with the simulated FR II jets, the spines shrink to $R_{\mathrm{sp}} \sim 0.5{-}0.7R_0$ with expanding sheaths of $W_{\mathrm{sh}} \sim 0.7{-}2R_0$, and the magnetic field increases in the sheath and piles up near the sheath edge. In contrast to the case for FR II jets, the magnetic field decreases more in spines with lower magnetization. The velocity profiles are smoothly decreasing in the sheaths, although they can be quite different in the spines. In the magnetic-pressure-dominated case (V6B-1), the spine velocity profile has an inflection point, although its magnetic field profile deviates only slightly from the initial configuration. On the other hand, in the V6B-2 and V6B-3 cases, where the gas pressure is important, the spine velocity profiles are flat.

Downloaded from https://academic.oup.com/mnras/article/519/2/1872/6965859 by DESY-Zentralbibliothek user on 03 February 2023

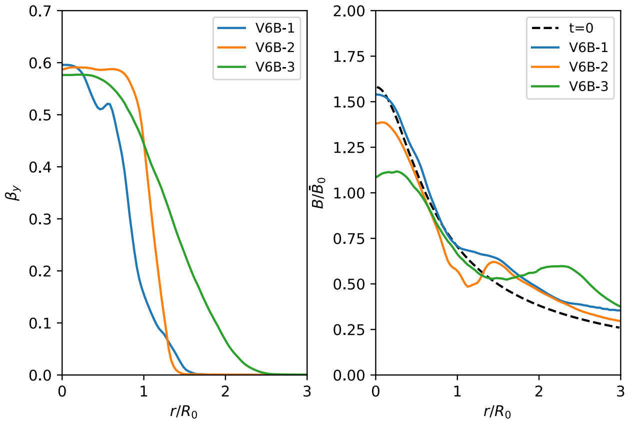

Figure 8. The velocity profiles (left-hand panel) and magnetic field profiles (right-hand panels) are presented for FR I jets at $t = 90R_0/c$ (V6B-1), $t = 100R_0/c$ (V6B-2), and $t = 120R_0/c$ (V6B-3). The magnetic field is normalized with $\bar{B}_0 = \sqrt{2\sigma}B_0$.

Overall, the velocity profile in the KHI-saturation stage is flat in the spine for most cases, and decreases smoothly in the sheath, with a roughly linear profile over much of its width. In the deep saturation regime, the sheath size is wider than the spine; that is, $W_{\rm sh} \gtrsim R_{\rm sp}$. In general, in the KHI-saturation stage a higher velocity leads to a wider sheath for fixed magnetization, while for fixed velocities the gas-pressure-dominated jet has the widest sheath.

3.2 Turbulence

We next examine the energy spectra of the jet velocity and the magnetic field in the KHI saturation stage. To enable comparison with the Fokker–Planck approach of Wang et al. (2021), we perform a fast Fourier transform (FFT) of the fluctuating velocity and magnetic fields along the jet axis with wavenumber $k_\parallel = 2\pi/\lambda$, where λ is the corresponding wavelength. The minimum wavenumber ($k_{\parallel,\rm min}$) thus corresponds to the wavelength λ equal to the simulation box size (see Table 1).

The magnetic turbulence is normalized according to the Alfvén velocity $\beta_{\rm A} = B/\sqrt{4\pi\Gamma\rho}c$, where B is the magnitude of the magnetic field in each computational cell. This allows us to make a straightforward comparison with the FFT of the magnitude of the velocity field. We consider the turbulence inside the spine ($r \le 0.7R_0$ for the simulated FR I jets) as well as in the spine-sheath region. For the latter, we include the data within $2.5R_0$ for FR I jets, and within $3.7R_0$ for FR II jets. The FFT analyses are performed for both FR I and FR II jets with different magnetizations. The results are shown in Figs 9 and 10. Owing to the limited dynamic range of the simulation, the spectrum covers only two orders of magnitude in $k_\parallel$. The roll-over at high wavenumbers, $k_\parallel R_0/2\pi \gtrsim 6$, is an artefact of the limited spatial resolution of the simulations.

In the range of $k_\parallel R_0/2\pi \lesssim 6$, the power spectrum of the velocity field is found to be approximately consistent with Kolmogorov-type turbulence for all cases, $P(k_\parallel) \propto k_\parallel^{-5/3}$. The magnetic power spectra are noticeably flatter at small $k_\parallel$ in virtually all cases, as the KHI-driven field fluctuations are concentrated on sub-jet-radius scales. At larger $k_\parallel$, the magnetic and kinetic power spectra converge. We anticipate that with increased spatial resolution, both the magnetic and the velocity field power spectra would extend to larger $k_\parallel$ with Kolmogorov scaling.

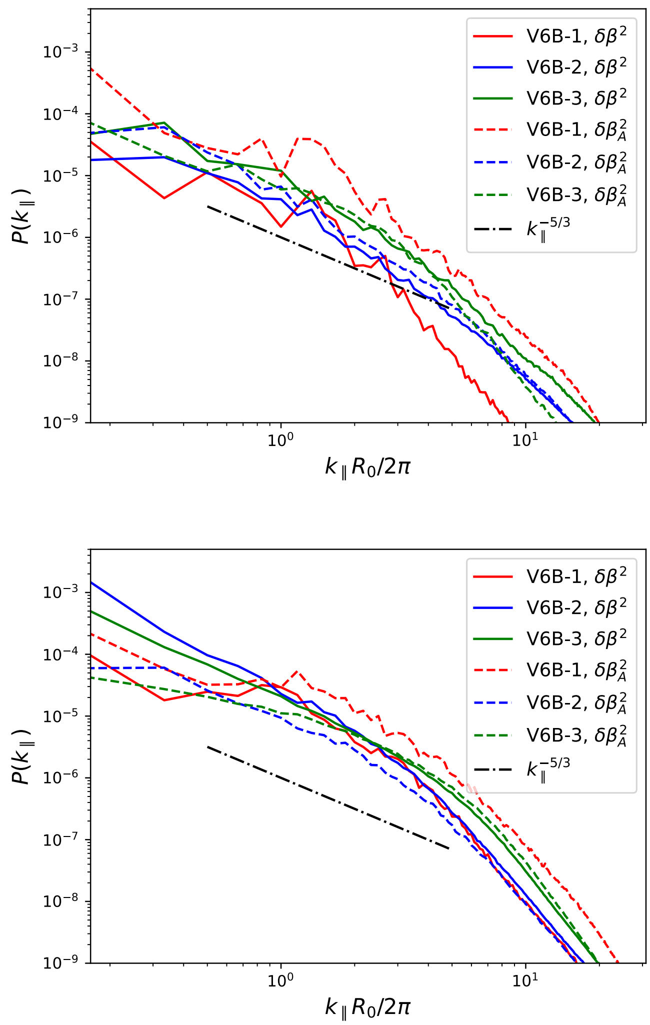

Figure 9. 1D axial turbulence spectra of simulated FR I jet spines within $r = 0.6,\ 0.7,\ 0.5R_0$ (top panel) and their spine-sheaths within $r = 1.5$, 1.4, $2.5R_0$ (bottom panel) are presented for cases V6B-1, V6B-2, and V6B-3, respectively. The solid lines trace the power spectrum of the turbulent velocity field $\delta\beta$, and the dashed lines show the power spectrum of the turbulent Alfvén velocity $\delta\beta_{\rm A}$, which we take to represent the turbulent magnetic field. For comparison, we also show the benchmark Kolmogorov-type $k_\parallel^{-5/3}$ turbulence.

The amplitudes of the velocity field power spectra at a given $k_\parallel$ vary slightly for different magnetizations and jet velocities, with amplitudes at the minimum wavenumber being $\delta\beta^2(k_{\parallel,\rm min}) \sim (10^{-3}–10^{-4})$ for the spine-sheath jets, as shown in Figs 9 and 10. The turbulent magnetic energy density is slightly higher than the turbulent kinetic energy density in the V6B-1 and V9B-1 cases and lower in other cases, but overall they are roughly comparable. Figs 9 and 10 also show that the highest-magnetization cases have the lowest turbulent kinetic energy, and the magnetic turbulence is enhanced on small scales in the lowest-magnetization cases.

In the top and bottom panels of Fig. 9, we show the turbulence spectra in the spine and spine-sheath of the simulated FR I jets, respectively. We find that the turbulence is well developed in both the spine and the sheath region. In the top panel of Fig. 10, we show the turbulent spectra in the spine-sheath of FR II jets, whose behaviours are similar to those of FR I jets. The bottom panel of Fig. 10 compares turbulent spectra with the same magnetization

Downloaded from https://academic.oup.com/mnras/article/519/2/1872/6965859 by DESY-Zentralbibliothek user on 03 February 2023

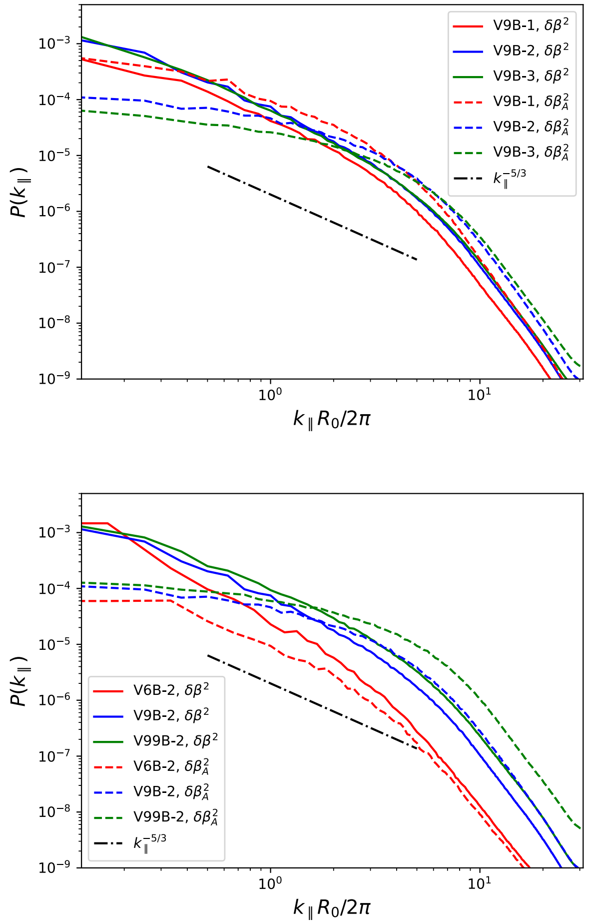

Figure 10. 1D axial turbulent spectra of simulated FR II jets within $r = 2.5,\ 2.1,\ 3.7R_0$ (top panel) for the V9B-1, V9B-2, and V9B-3 cases and simulated jets with a fixed magnetization parameter but different velocities (bottom panel). The jet width of the V99B-2 case is chosen to be $r = 2.8R_0$. The solid lines are for the turbulent velocity field $\delta\beta$, and the dashed lines are for the turbulent Alfvén velocity field $\delta\beta_{\rm A}$. For comparison, we also show the benchmark Kolmogorov-type $k_\parallel^{-5/3}$ turbulence.

but different velocities. This shows that the turbulent magnetic and kinetic energy densities are larger in higher-velocity jets.

3.3 Particle spectral index of shear acceleration

Following our previous paper (Wang et al. 2021; Rieger & Duffy 2021, 2022), the spectral index of the accelerated particle distribution, $n(\gamma) \propto \gamma^s$, in the leaky-box framework for gradual shear acceleration is

$$s = \frac{q-1}{2} - \sqrt{\frac{(q-5)^2}{4} + w}, \tag{6}$$

which depends on the turbulence spectrum $k_\parallel^{-q}$, and we find $q \approx 5/3$ for most cases in our simulations. The shear coefficient, w, is determined by the region (Δr) that confines the particles, and the flow velocity profile $\beta_y(r)$, as

$$w = \frac{10}{\Gamma^4(r)\Delta r^2}\left(\frac{\partial \beta_y(r)}{\partial r}\right)^{-2}, \tag{7}$$

where $\Gamma(r)$ is the jet-flow Lorentz factor. To approximate spatial transport, we replace w by an averaged shear coefficient ($\bar{w}$) for cylindrical jets, defined here as the average of $<\Gamma^2(r)\partial\beta_y(r)/\partial r>$ over r, with $<f> = \int rf{\rm d}r/\int r{\rm d}r$. Other averaging methods have been explored by assuming a linearly decreasing profile (Rieger & Duffy 2019) and non-linear-type profiles (Rieger & Duffy 2022) in the sheath.

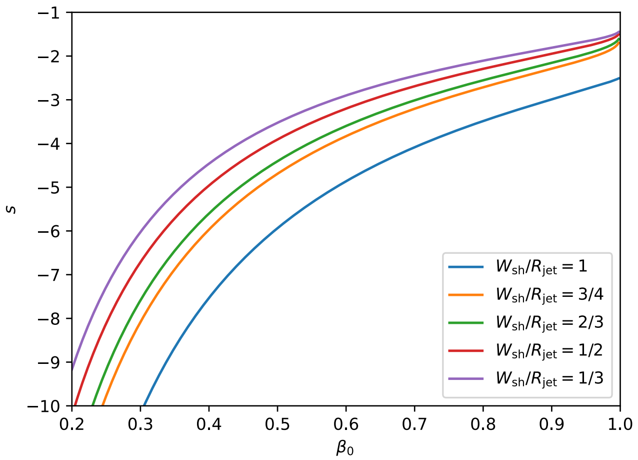

Figure 11. Spectral index of a shear-accelerated particle distribution, $n(\gamma) \propto \gamma^s$, for various ratios of $W_{\rm sh}/R_{\rm jet} = 1,\ 1/2,\ 1/3,\ 1/4$ and spine velocities.

We approximate our simulation results as a simple velocity profile with $\beta_y = \beta_0$ inside the spine ($r \le R_{\rm sp}$) and $\beta_y = \beta_0(R_{\rm jet} - r)/(W_{\rm sh})$ in the sheath, with $R_{\rm jet} = R_{\rm sp} + W_{\rm sh}$ being the total jet radius. As particles entering the spine could re-enter the sheath again, and as turbulence is well developed in both the spine and the sheath, here we consider $\Delta r = R_{\rm jet}$. This then yields

$$\bar{w} = \frac{10\beta_0^2}{[\ln \Gamma_0^{-2} W_{\rm sh} R_{\rm jet}^{-1} + 2\beta_0 \tanh^{-1}(\beta_0)]^2}. \tag{8}$$

For $\beta_0 \rightarrow 1$, we have $w \rightarrow 0$ and $s \rightarrow -4/3$.

In Fig. 11, we show the resultant spectral index of the accelerated particles for various values of $W_{\rm sh}/R_{\rm jet}$, where the blue line ($W_{\rm sh} = R_{\rm jet}$) is equivalent to the case that only considers the sheath. We find that for a given velocity, the spectrum is harder for a narrower sheath, and in the highly relativistic limit, the spectral index is less dependent on the velocity profile, consistent with Rieger & Duffy (2022).

From our simulation results, we find $W_{\rm sh}/R_{\rm jet} \sim 1/4{-}1/2$ in the transition stage and $W_{\rm sh}/R_{\rm jet} \sim 1/2{-}4/5$ in the deep saturation stage for FR I/II jets, depending on the magnetization and the velocity. In our previous studies, estimates of the magnetic field and the coefficient $\bar{w}$ were obtained for 3C 273 and Centaurus A by fitting their multiwavelength SEDs (see table 1 of Wang et al. 2021). Our results here suggest that Centaurus A and 3C 273 can be approximately described by the V6B-2 case and V9B-3 case, respectively. Taking $W_{\rm sh}/R_{\rm jet} = 1/2\ (3/4)$ for Centaurus A (3C 273), $\bar{w} = 15\ (4.7)$ requires $\beta_0 = 0.5\ (0.87)$. These velocities are consistent with radio observations, which indicate $\beta_0 \sim 0.5$ for Centaurus A (Hardcastle et al. 2003; Snios et al. 2019) and $\beta_0 < 0.94$ for 3C 273 (Meyer et al. 2016).

4 CONCLUSION AND DISCUSSION

Particle acceleration in shearing flows depends on the underlying flow velocity profile and turbulence properties. In this paper, we have studied such properties in self-generated spine-sheaths through RMHD simulations. By propagating a relativistic spine through a

Downloaded from https://academic.oup.com/mnras/article/519/2/1872/6965859 by DESY-Zentralbibliothek user on 03 February 2023

static cocoon, we observe that a sheath is formed at the interface, mainly owing to the KHI. We find that, in general, a higher velocity or a lower magnetization leads to a wider sheath, and in the transition and saturation stage of the KHI, the simulated FR I/II jets have sheath widths $W_{\rm sh}/R_{\rm jet} \sim 1/4-1/2$ and $W_{\rm sh}/R_{\rm jet} \sim 1/2-4/5$, respectively. The averaged velocity is approximately constant in the spine and shows a smooth (approximately linear) decrease in the sheath.

The development of turbulence is seen in both the spine and the sheath. The turbulent velocity field shows a rather good agreement with Kolmogorov-type behaviour in all cases, independent of the initial velocity and magnetization. The magnetic field, on the other hand, reveals some dependence on magnetization has a flatter turbulence spectrum. In general, we find that the turbulent magnetic energy is roughly comparable to the turbulent kinetic energy.

The inferred flow properties have been used to explore the potential of shear particle acceleration in large-scale AGN jets. Assuming a quasi-linearly decreasing profile in the sheath, the spine velocities required to reproduce the observed X-ray spectra are found to be compatible with values reported for Centaurus A and 3C 273. We note that our simulations provide indications that the velocity profiles of the spine/sheath before averaging can be more complex; see, for example, Figs 2 and 3. A higher velocity gradient in some local region could enhance the efficiency of shear acceleration. A quantification of this is, however, beyond the scope of the present paper, and is left to future test-particle simulations.

From a phenomenological perspective, one of the major challenges in understanding the FR dichotomy is that most of the observed SEDs of FR I jets can be explained by a single population of electrons (e.g. Perlman et al. 2001; Hardcastle, Birkinshaw & Worrall 2001; Sun et al. 2018), while two populations of electrons seem to be required to account for the SEDs of FR II jets (e.g. Jester et al. 2006; Hardcastle, Kraft & Worrall 2006). One interesting possibility is that shocks formed during the KHI development provide seed particles for shear acceleration to generate a second population of electrons. To investigate this, we also searched for shocks in our simulations following the approach in Mukherjee et al. (2020, 2021). We found shocks in the KHI-saturation stage primarily in the lowest-magnetization cases, $\sigma = 10^{-3}$. Because, as our results indicate, Centaurus A and 3C 273 may be approximately described by the V6B-2 and the V9B-3 case, respectively, this would suggest that a second population of electrons should be present only in 3C 273, which would be consistent with observations. In our simulations, however, these shocks seem to occupy only a very small volume compared with the whole simulation domain. Because this outcome might be affected by our choice of periodic boundary conditions, further high-resolution, full jet propagation studies will be needed to reach a firm conclusion on this possibility. This will also help in gaining a better understanding of the formation of knots and the possibility of variable X-ray emission in large-scale AGN jets.

ACKNOWLEDGEMENTS

We thank the referee for helpful suggestions, and Eileen Meyer, Zhi Li, Omer Bromberg, and Krzysztof Nalewajko for helpful discussions. JSW acknowledges support from the Alexander von Humboldt Foundation. YM acknowledges support from the National Natural Science Foundation of China (grant no. 12273022) and Shanghai pilot program of international scientist for basic research (grant no. 22JC1410600). FMR acknowledges support from a DFG Fellowship (RI 1187/8-1). The simulations were run on the high-performance computing cluster at the Max-Planck-Institut für Kernphysik.

DATA AVAILABILITY

The data underlying this article will be shared on reasonable request to the corresponding author.

REFERENCES

Baty H., Keppens R., 2002, ApJ, 580, 800
Berezhko E. G., 1981, ZhETF Pisma Redaktsiiu, 33, 416
Berezhko E. G., Krymskii G. F., 1981, Soviet Astron. Lett., 7, 352
Birkinshaw M., 1991, MNRAS, 252, 505
Blandford R., Meier D., Readhead A., 2019, ARA&A, 57, 467
Boccardi B., Krichbaum T. P., Bach U., Mertens F., Ros E., Alef W., Zensus J. A., 2016, A&A, 585, A33
Bodo G., Mamatsashvili G., Rossi P., Mignone A., 2013, MNRAS, 434, 3030
Bodo G., Mamatsashvili G., Rossi P., Mignone A., 2019, MNRAS, 485, 2909
Borse N., Acharya S., Vaidya B., Mukherjee D., Bodo G., Rossi P., Mignone A., 2021, A&A, 649, A150
Breiding P., Meyer E. T., Georganopoulos M., Keenan M. E., DeNigris N. S., Hewitt J., 2017, ApJ, 849, 95
Bromberg O., Singh C. B., Davelaar J., Philippov A. A., 2019, ApJ, 884, 39
Cara M. et al., 2013, ApJ, 773, 186
Chow A., Davelaar J., Sironi L., 2022, preprint (arXiv:2209.13699)
Earl J. A., Jokipii J. R., Morfill G., 1988, ApJ, 331, L91
Ferrari A., Trussoni E., Zaninetti L., 1978, A&A, 64, 43
Gabuzda D. C., Reichstein A. R., O'Neill E. L., 2014, MNRAS, 444, 172
Georganopoulos M., Meyer E., Perlman E., 2016, Galaxies, 4, 65
Gourgouliatos K. N., Komissarov S. S., 2018, Nat. Astron., 2, 167
H. E. S. S. Collaboration et al., 2020, Nature, 582, 356
Hardcastle M. J., Birkinshaw M., Worrall D. M., 2001, MNRAS, 326, 1499
Hardcastle M. J., Worrall D. M., Kraft R. P., Forman W. R., Jones C., Murray S. S., 2003, ApJ, 593, 169
Hardcastle M. J., Kraft R. P., Worrall D. M., 2006, MNRAS, 368, L15
Hardee P. E., 1979, ApJ, 234, 47
Hardee P. E., 2007, ApJ, 664, 26
Harris D. E., Krawczynski H., 2006, ARA&A, 44, 463
Jester S., Harris D. E., Marshall H. L., Meisenheimer K., 2006, ApJ, 648, 900
Kim J., Balsara D. S., Lyutikov M., Komissarov S. S., 2018, MNRAS, 474, 3954
Komissarov S. S., 1999, MNRAS, 308, 1069
Laing R. A., Bridle A. H., 2014, MNRAS, 437, 3405
Liu R.-Y., Rieger F. M., Aharonian F. A., 2017, ApJ, 842, 39
Lyubarskii Y. E., 1999, MNRAS, 308, 1006
Martí J.-M., 2019, Galaxies, 7, 24
Martí J. M., Müller E., Font J. A., Ibáñez J. M. Z., Marquina A., 1997, ApJ, 479, 151
Mathews W. G., 1971, ApJ, 165, 147
Meyer E. T., Georganopoulos M., 2014, ApJ, 780, L27
Meyer E. T., Georganopoulos M., Sparks W. B., Godfrey L., Lovell J. E. J., Perlman E., 2015, ApJ, 805, 154
Meyer E. T. et al., 2016, ApJ, 818, 195
Mignone A., Plewa T., Bodo G., 2005, ApJS, 160, 199
Mignone A., Bodo G., Massaglia S., Matsakos T., Tesileanu O., Zanni C., Ferrari A., 2007, ApJS, 170, 228
Mignone A., Rossi P., Bodo G., Ferrari A., Massaglia S., 2010, MNRAS, 402, 7
Mizuno Y., Hardee P., Nishikawa K.-I., 2007, ApJ, 662, 835
Mizuno Y., Lyubarsky Y., Nishikawa K.-I., Hardee P. E., 2009, ApJ, 700, 684
Mizuno Y., Lyubarsky Y., Nishikawa K.-I., Hardee P. E., 2012, ApJ, 757, 16
Mizuno Y., Hardee P. E., Nishikawa K.-I., 2014, ApJ, 784, 167
Mukherjee D., Bodo G., Mignone A., Rossi P., Vaidya B., 2020, MNRAS, 499, 681
Mukherjee D., Bodo G., Rossi P., Mignone A., Vaidya B., 2021, MNRAS, 505, 2267

Downloaded from https://academic.oup.com/mnras/article/519/2/1872/6965859 by DESY-Zentralbibliothek user on 03 February 2023

Nagai H. et al., 2014, ApJ, 785, 53

Nakamura M., Li H., Li S., 2007, ApJ, 656, 721

Ortuño-Macías J., Nalewajko K., Uzdensky D. A., Begelman M. C., Werner G. R., Chen A. Y., Mishra B., 2022, ApJ, 931, 137

Perlman E. S., Biretta J. A., Sparks W. B., Macchetto F. D., Leahy J. P., 2001, ApJ, 551, 206

Perlman E. S., Clautice D., Avachat S., Cara M., Sparks W. B., Georganopoulos M., Meyer E., 2020, Galaxies, 8, 71

Perucho M., Martí J. M., 2007, MNRAS, 382, 526

Perucho M., Hanasz M., Martí J. M., Sol H., 2004, A&A, 427, 415

Perucho M., Martí J.-M., Quilis V., 2019, MNRAS, 482, 3718

Rieger F. M., 2019, Galaxies, 7, 78

Rieger F. M., Duffy P., 2004, ApJ, 617, 155

Rieger F. M., Duffy P., 2016, ApJ, 833, 34

Rieger F. M., Duffy P., 2019, ApJ, 886, L26

Rieger F. M., Duffy P., 2021, ApJ, 907, L2

Rieger F. M., Duffy P., 2022, ApJ, 933, 149

Rieger F. M., Bosch-Ramon V., Duffy P., 2007, Ap&SS, 309, 119

Rossi P., Mignone A., Bodo G., Massaglia S., Ferrari A., 2008, A&A, 488, 795

Rossi P., Bodo G., Capetti A., Massaglia S., 2017, A&A, 606, A57

Scheck L., Aloy M. A., Martí J. M., Gómez J. L., Müller E., 2002, MNRAS, 331, 615

Sironi L., Rowan M. E., Narayan R., 2021, ApJ, 907, L44

Snios B. et al., 2019, ApJ, 871, 248

Sun X.-N., Yang R.-Z., Rieger F. M., Liu R.-Y., Aharonian F., 2018, A&A, 612, A106

Tavecchio F., 2021, MNRAS, 501, 6199

Tchekhovskoy A., Bromberg O., 2016, MNRAS, 461, L46

Wang J.-S., Reville B., Liu R.-Y., Rieger F. M., Aharonian F. A., 2021, MNRAS, 505, 1334

Webb G. M., Barghouty A. F., Hu Q., le Roux J. A., 2018, ApJ, 855, 31

Webb G. M., Al-Nussirat S., Mostafavi P., Barghouty A. F., Li G., le Roux J. A., Zank G. P., 2019, ApJ, 881, 123

Webb G. M., Mostafavi P., Al-Nussirat S., Barghouty A. F., Li G., le Roux J. A., Zank G. P., 2020, ApJ, 894, 95

This paper has been typeset from a TEX/LATEX file prepared by the author.

Downloaded from https://academic.oup.com/mnras/article/519/2/1872/6965859 by DESY-Zentralbibliothek user on 03 February 2023